

Large Einstein Radii: A Problem for Λ CDM

Tom J. Broadhurst¹ and Rennan Barkana^{2,3*}

¹*Raymond and Beverly Sackler School of Physics and Astronomy, Tel Aviv University, Tel Aviv 69978, Israel*

²*Institute for Cosmic Ray Research, University of Tokyo, Kashiwa 277-8582, Japan*

³*Guggenheim Fellow; on sabbatical leave from the School of Physics and Astronomy, Tel Aviv University, Israel*

9 March 2019

ABSTRACT

The Einstein radius of a cluster provides a relatively model-independent measure of the mass density of a cluster within a projected radius of ~ 150 kpc, large enough to be relatively unaffected by gas physics. We show that the observed Einstein radii of four well-studied massive clusters, for which reliable virial masses are measured, lie well beyond the predicted distribution of Einstein radii in the standard Λ CDM model. Based on large samples of numerically simulated cluster-sized objects with virial masses $\sim 10^{15} M_{\odot}$, the predicted Einstein radii are only $15 - 25''$, a factor of two below the observed Einstein radii of these four clusters. This is because the predicted mass profile is too shallow to exceed the critical surface density for lensing at a sizable projected radius. After carefully accounting for measurement errors as well as the biases inherent in the selection of clusters and the projection of mass measured by lensing, we find that the theoretical predictions are excluded at a $4\text{-}\sigma$ significance. Since most of the free parameters of the Λ CDM model now rest on firm empirical ground, this discrepancy may point to an additional mechanism that promotes the collapse of clusters at an earlier time thereby enhancing their central mass density.

Key words: galaxies: clusters: general – cosmology:theory – galaxies:formation – cosmological parameters – dark matter

1 INTRODUCTION

The standard picture of the basic cosmological framework has recently come to rest firmly on detailed empirical evidence regarding the cosmological parameters, the proportions of baryonic and non-baryonic dark matter, together with the overall shape and normalization of the power spectrum (e.g., Astier et al. 2006; Spergel et al. 2007; Percival et al. 2007). This framework has become the standard Λ CDM cosmological model, with the added simple assumptions that the dark matter reacts only to gravity, is initially sub-relativistic, and possesses initial density perturbations which are Gaussian distributed in amplitude. This is a very well defined and relatively simple model, with clear predictions which are amenable to examination with observations. The cooling history of baryons complicates the interpretation of dark matter on galaxy scales, especially for dwarf galaxies that traditionally have been a major focus of studies of halo structure. Clusters have the advantage that the virial temperature of the associated gas is too hot for efficient cooling, so the majority of the baryons must trace the overall gravitational potential and hence we may safely com-

pare lensing-based cluster mass measurements to theoretical predictions that neglect gas physics and feedback.

Lensing-based determinations of the mass profiles of galaxy clusters rely on detailed modeling of the strong lensing region to define the inner mass profile, and also a careful analysis of the outer weak lensing regime. The latter involves substantial corrections for instrumental and atmospheric effects (Kaiser et al. 1995), and a clear definition of the background, free of contamination by the lensing cluster (Broadhurst et al. 2005b; Medezinski et al. 2007). In the center we may make use of the Einstein radius of a cluster which is often readily visible from the presence of giant arcs and provides a relatively model-independent determination of the central mass density. In the case of axial symmetry, the projected mass inside the Einstein radius θ_E depends only on fundamental and cosmological constants: $M(< \theta_E) = \theta_E^2 (c^2/4G) D_{OL} D_{OS}/D_{LS}$, where this combination of angular diameter distances (observer-lens, observer-source, and lens-source) leads to a relatively weak dependence on the lens and source redshifts. More generally, an effective Einstein radius can be defined by axially averaging the projected surface density, which itself is well determined when there are a large number of constraints. Virtually all known massive clusters at intermediate redshifts,

* E-mail: tjb@wise.tau.ac.il; barkana@wise.tau.ac.il

$0.15 < z < 0.8$, show multiple images including obvious arcs in sufficiently deep high-resolution data. The derived Einstein radius of these massive clusters typically falls in the range $10'' < \theta_E < 20''$ (Gioia et al. 1990; Smith et al. 2005), with the largest known case of $\sim 50''$ for A1689.

Increasingly large simulations have helped to specify the evolution of the halo mass function and the form of the mass profile predicted in the context of the Λ CDM model (Navarro et al. 1997; Bullock et al. 2000). These simulations are now becoming sufficiently large and detailed to define the predicted spread of halo structure over a wide range of halo mass, and to quantitatively assess the inherent bias in observing clusters in projection and selecting them by lensing cross-section (Hennawi et al. 2007; Neto et al. 2007). For the most massive collapsed objects in these simulations (virial mass $M_{\text{vir}} \sim 10^{15} M_\odot$), a mean observed concentration of $c_{200} \sim 6$ is predicted for lenses, where c_{200} is defined precisely in the next section. Such profiles are relatively shallow and seem at odds with recent careful lensing studies of massive clusters; although the NFW profile provides acceptable fits to the observations, relatively high concentrations of $c_{\text{vir}} \sim 10 - 15$ are derived for several well-studied massive clusters (Kneib et al. 2003; Gavazzi et al. 2003; Broadhurst et al. 2005b; Kling et al. 2005; Limousin et al. 2007; Bradač et al. 2007; Halkola et al. 2008; Umetsu & Broadhurst 2008). These values are larger than expected based on simulations of the standard Λ CDM model. Given the relatively shallow mass profile predicted for cluster-mass CDM halos, the question arises whether the projected critical surface density for lensing can be exceeded within a substantial radius for this model.

In this paper we compare observations of well-constrained massive clusters with the predictions of Λ CDM simulations. While we make use of the NFW profile, our comparison of the theory and observations is mostly independent of profile fitting. In particular, the observed θ_E and the simulated M_{vir} are obtained directly, the simulated θ_E can easily be in future work (though here we calculate it using the NFW fits), and the observed M_{vir} is obtainable directly at least for one cluster: A1689. This paper is structured as follows. In section 2 we first summarize the theoretical predictions, including a brief review of the NFW profile and its lensing properties, and of the halo concentrations measured by Neto et al. (2007) and Hennawi et al. (2007) in large numerical simulations. Note that the conflict between high observed concentrations and lower ones determined for the numerical halos was noted in both of these papers (see also Williams et al. (1999)). We then present the observational data for the four clusters, followed by a model-independent method for measuring the mass, which we apply to A1689. In section 3 we confront the theoretical predictions with the data, finding a clear discrepancy. We discuss the possible implications in section 4.

2 THEORETICAL AND OBSERVATIONAL INPUTS

2.1 Theoretical Predictions

Our calculations are made in a cold dark matter plus cosmological constant (i.e., Λ CDM) universe matching observa-

tions (Spergel et al. 2007), with a power spectrum normalization $\sigma_8 = 0.826$, Hubble constant $H_0 = 100h \text{ km s}^{-1} \text{ Mpc}^{-1}$ with $h = 0.687$, spectral index $n = 0.957$, and present density parameters $\Omega_m = 0.299$, $\Omega_\Lambda = 0.701$, and $\Omega_b = 0.0478$ for matter, cosmological constant, and baryons, respectively. Unless otherwise indicated, we use physical units that already include the proper factors of h or h^{-1} , always with $h = 0.687$.

Consider a halo that virialized at redshift z in a flat universe with $\Omega_m + \Omega_\Lambda = 1$. At z , Ω_m has a value

$$\Omega_m^z = \frac{\Omega_m(1+z)^3}{\Omega_m(1+z)^3 + \Omega_\Lambda}, \quad (1)$$

and the critical density is

$$\rho_c^z = \frac{3H_0^2}{8\pi G} \frac{\Omega_m(1+z)^3}{\Omega_m^z}. \quad (2)$$

The mean enclosed virial density in units of ρ_c^z is denoted Δ_c and used to define the virial mass and radius in observations and in simulations. Sometimes a fixed value is used, such as $\Delta_c = 200$, although the theoretical value is $\Delta_c = 18\pi^2 \simeq 178$ in the Einstein-de Sitter model, modified in a flat Λ CDM universe to the fitting formula (Bryan & Norman 1998)

$$\Delta_c = 18\pi^2 + 82d - 39d^2, \quad (3)$$

where $d \equiv \Omega_m^z - 1$. A halo of mass M collapsing at redshift z thus has a (physical) virial radius

$$r_{\text{vir}} = 1.69 \left(\frac{M}{10^{15} M_\odot} \right)^{1/3} \left[\frac{\Omega_m h^2}{\Omega_m^z} \frac{\Delta_c}{18\pi^2} \right]^{-1/3} \frac{1}{1+z} \text{ Mpc}. \quad (4)$$

Numerical simulations of hierarchical halo formation indicate a roughly universal spherically-averaged density profile for virialized halos (Navarro et al. 1997), though with considerable scatter among different halos (e.g., Bullock et al. 2000). The NFW profile has the form

$$\rho(r) = \rho_c^z \frac{\delta_c}{x(1+x)^2}, \quad (5)$$

where $x = r/r_s$ in terms of the NFW scale radius $r_s = r_{\text{vir}}/c_{\text{vir}}$, and the characteristic density δ_c is related to the concentration parameter c_{vir} by

$$\delta_c = \frac{\Delta_c}{3} \frac{c_{\text{vir}}^3}{\ln(1+c_{\text{vir}}) - c_{\text{vir}}/(1+c_{\text{vir}})}. \quad (6)$$

For a halo of mass M at a given redshift z , the profile is fixed once we know Δ_c and c_{vir} . In this paper we denote the concentration parameter, virial radius and mass by c_{vir} , r_{vir} and M_{vir} when using the theoretical value in equation (3), and by c_{200} , r_{200} , and M_{200} , respectively, when using $\Delta_c = 200$.

The lensing properties of a halo are determined by κ , the projected surface density Σ measured in units of the critical surface density $\Sigma_{\text{cr}} = [c^2/(4\pi G)] D_{\text{OS}}/(D_{\text{OL}} D_{\text{LS}})$. For an axisymmetric lens, the Einstein radius (i.e., tangential critical curve) occurs at a projected radius R where the mean enclosed surface density satisfies $\bar{\kappa}(R) = 1$. For an NFW halo, letting $X = R/r_s$ we have $\bar{\kappa}(X) = (4/\Sigma_{\text{cr}}) \rho_c^z \delta_c r_s g(X)/X^2$ where (Bartelmann 1996)

$$g(x) = \ln \frac{x}{2} + \begin{cases} 1, & x = 1 \\ \frac{2}{\sqrt{x^2-1}} \tan^{-1} \sqrt{\frac{x-1}{x+1}}, & x > 1 \\ \frac{2}{\sqrt{1-x^2}} \tanh^{-1} \sqrt{\frac{1-x}{1+x}}, & x < 1 \end{cases}. \quad (7)$$

We derive the theoretical predictions for cluster lensing in Λ CDM by combining the two largest studies of halo structure in cosmological numerical simulations. Neto et al. (2007) studied halo structure within the Millennium simulation, in which over 2000 halos formed with $M_{200} > 10^{14} M_{\odot}$ at $z = 0$. Each halo was resolved with $> 80,000$ particles, allowing a detailed look at its three-dimensional density structure using NFW profile fitting. This is therefore the best available statistical analysis of the cluster halo population in Λ CDM simulations. However, since Neto et al. (2007) did not study projected halo profiles or the bias in selecting lenses, we must adjust their results in order to apply them to lensing. Hennawi et al. (2007) studied 900 simulated cluster halos at $z = 0.41$, each resolved into at least 30,000 particles. They studied projections through on average 15 random directions per cluster (more – up to 125 – for the most massive ones), and fit both 3-D and projected 2-D NFW profiles. Moreover, they separately studied the distribution of NFW profile parameters both for the general halo population and for the lensing population (i.e., where halos are weighted by their strong lensing cross section). They showed that the inherent triaxiality of CDM halos along with the presence of substructure enhance the projected mass in some orientations, leading to a bias in the 2-D structure of lenses compared with the 3-D structure of the general population of cluster halos (see also Oguri et al. (2005)).

Figure 1 shows various biases in halo concentration parameters c_{vir} as measured by Hennawi et al. (2007). The Figure shows (left panel) that the distribution of 3-D concentrations of the lens population is the same as that of the general halo population except for a shift upwards by a factor of 1.17. For a given real 3-D profile, the 2-D profile measured in projection depends on the orientation, and is thus given by a probability distribution. The Figure also shows (right panel) that the ratio c_{2-D}/c_{3-D} follows a log-normal distribution, i.e., that \log_{10} of this ratio is well fitted by a Gaussian with a mean value of 0.057 and $\sigma = 0.124$, which correspond to factors of 1.14 and 1.33, respectively.

At $z = 0.41$, r_{200} and c_{200} are typically $\sim 15\%$ smaller than r_{vir} and c_{vir} , respectively, and $M_{200} \approx 0.9M_{\text{vir}}$. We assume that the *relative* distributions shown in Figure 1 are approximately the same for c_{200} as for c_{vir} , and that they are independent of halo mass within the narrow range considered, as found by Hennawi et al. (2007). Thus, we can apply these findings to convert the 3-D c_{200} distributions measured by Neto et al. (2007) in order to obtain the resulting 2-D projected distributions of c_{200} values for the population of cluster lenses. Specifically, we multiply the c_{200} values by a factor of 1.17 (the lensing bias) and then convolve with the distribution of c_{2-D}/c_{3-D} for lenses (the projection bias). Note that we use the values measured by Neto et al. (2007) at $z = 0$ when comparing to the observed clusters at redshifts $z = 0.18 - 0.40$. This is a conservative assumption, since the typical concentration parameter at a given halo mass declines with redshift. A study based on the Millennium simulation (Gao et al. 2007) found a relatively weak decline of $\sim 20\%$ out to $z = 1$, which suggests a 5 – 10% decline out to the redshifts we consider below, a decline which we do not include here.

In Figure 2 we show the predicted Einstein radii of Λ CDM cluster halos of mass $M_{200} > 10^{14} M_{\odot}$ based on Neto et al. (2007) and Hennawi et al. (2007). Neto et al. (2007)

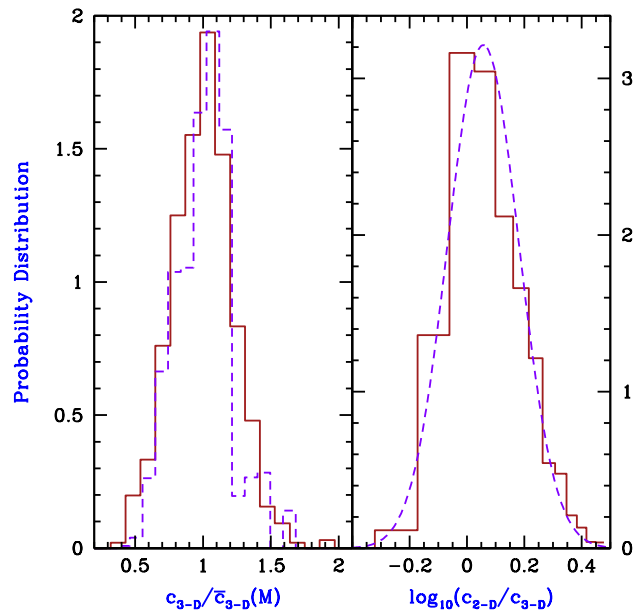


Figure 1. Probability distributions of various concentration parameters, based on Hennawi et al. (2007). *Left panel:* When the concentration parameters are measured relative to the median at each halo mass (Figure 8 of Hennawi et al. (2007)), the distribution for the general population (solid histogram) matches that for the lens population when the latter is divided by a factor of 1.17 (dashed histogram). *Right panel:* For lensing halos, the distribution of \log_{10} of the ratio of the 2-D to the 3-D concentration (solid histogram) is well fitted by a Gaussian with the same mean and variance as the histogram (dashed curve). Note that the non-uniform binning is a result of our conversion of the linear-axis histogram from Figure 12 of Hennawi et al. (2007) to one with a logarithmic x -axis.

divided their halos within each mass bin into “relaxed” and “unrelaxed” groups of halos, the latter identified as being disturbed dynamically as indicated by a large amount of substructure, a large offset between the center of mass and the potential center, or a high kinetic energy relative to potential. For each group, they found that the statistical distribution of the concentration parameters was well-fitted by a lognormal distribution. Thus, after correcting for lensing and projection bias as explained above, the resulting distributions remain lognormal. As shown in Figure 2, the median c_{200} of each group is only weakly dependent on mass, showing a slight trend of decreasing concentration with increasing halo mass (a trend which is more apparent over the broader range considered by Neto et al. (2007), down to $M_{200} = 10^{12} M_{\odot}$). As a result, we find that $\theta_E \propto M_{200}$ (relaxed) and $\theta_E \propto (M_{200})^{1.6}$ (unrelaxed). Note that for a lognormal distribution, the median and mean are theoretically the same if $\log_{10} c_{200}$ is considered rather than c_{200} . As the Figure shows, the typical scatter in $\log_{10} c_{200}$ among halos of the same mass is also fairly independent of mass, except for the highest mass bin, $M_{200} > 10^{15} M_{\odot}$. While this bin is based on a somewhat small sample (8 relaxed and 11 unrelaxed halos), Neto et al. (2007) suggest that the lower dispersion is expected since the highest-mass halos are very rare, thus all formed very recently and should have similar merger histories and thus internal structures. Note that the

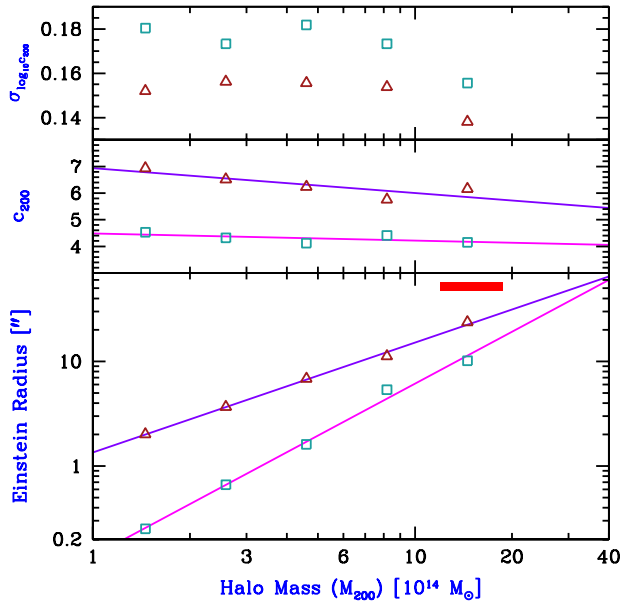


Figure 2. Dependence of θ_E (bottom panel), the median c_{200} (middle panel), and the scatter $\sigma_{\log_{10}c_{200}}$ (top panel) on halo mass M_{200} in numerical simulations. We use the 3-D analysis by Neto et al. (2007) corrected for lensing and projection bias based on Figure 1. We consider the relaxed (triangles) or unrelaxed (squares) halo populations. We assume the median c_{200} and the A1689 redshifts when calculating r_E . We show several linear least-squares fits to help discern trends (solid curves). Also shown for comparison (narrow box, bottom panel) is the location corresponding to the observations of A1689 (where the boxed area contains the two-sided 1- σ ranges of M_{200} and θ_E).

final, effective scatter in our calculations is only $\sim 10\%$ lower for the last bin compared with the lower mass bins, since we assume that the projection scatter is independent of halo mass.

2.2 Observational Data

For our data set of lensing clusters we choose four well-studied clusters with strong constraints available both from multiply-imaged arcs in the strong-lensing regime and from distorted arcs and magnification measurements in the weak-lensing regime. We determine an effective Einstein radius in each cluster using the 2-D projected mass distribution obtained from fitting (without assuming symmetry) to the large number of sets of multiple images; from the obtained κ we then define θ_E in the standard way, as the radius enclosing a mean surface density equal to the critical surface density for lensing. Note that this definition effectively axially averages the mass distribution. We can define θ_E relative to any source redshift, and in each cluster we choose a fiducial redshift that matches a prominent arc system. Our procedure for determining θ_E is also a good match to that followed by Hennawi et al. (2007) for their simulated clusters, where they fit an axially symmetric model to the projected mass distribution; we obtain the predicted effective Einstein radii of the simulated clusters based on their model fits, as detailed in the previous subsection. For the observed clusters,

Table 1. Observational Data

Cluster	$M_{\text{vir}} [M_{\odot}]$	$M_{200} [M_{\odot}]$	$\theta_E ["]$	z_L	z_S
A1689	1.6×10^{15}	1.5×10^{15}	52	0.183	3
Cl0024-17	8.7×10^{14}	8.0×10^{14}	31	0.395	1.7
A1703	1.0×10^{15}	9.0×10^{14}	32	0.258	2.8
RXJ1347	1.3×10^{15}	1.2×10^{15}	35	0.45	1.8

we also obtain effective virial masses from combined axially-symmetric fits to the strong and weak lensing data.

Very deep HST/ACS imaging of several massive lensing clusters has been obtained by the ACS/GTO team (Ford et al. 1998). This includes the well-studied cluster A1689 ($z = 0.183$) for which several comprehensive strong lensing analyses have been published. The analysis of Broadhurst et al. (2005a) identified over 100 multiply lensed images of 30 background galaxies by an iterative procedure in which multiple images are securely identified by delensing and relensing background galaxies. These multiple images have been used as a basis for other types of modeling, including fully parametric (Halkola et al. 2006; Zekser et al. 2006; Limousin et al. 2007) and non-parametric modeling (Diego et al. 2005). Broadhurst et al. (2005b) combined these data on the inner mass profile with wide field archival Subaru images and obtained a detailed radial mass profile for the entire cluster, finding an NFW-like projected mass profile with a surprisingly high value for the concentration parameter ($c_{\text{vir}} = 13.7 \pm 1.2$), and a virial mass of $M_{\text{vir}} = (1.9 \pm 0.2) \times 10^{15} M_{\odot}$ (the value in Table 1 is different; see the next subsection). This yields an effective Einstein radius of $52''$ at a fiducial redshift $z = 3$, in good agreement with the radius of $\sim 50''$ found for prominent multiple arcs at this redshift. We adopt a conservative error estimate of 10% on θ_E for all the clusters (Table 1). Note that an Einstein radius of only $31''$ is implied by the NFW fit of Limousin et al. (2007) to independent weak lensing data from CFHT, but this number is incompatible with their own strong lensing analysis and is possibly caused by contamination of the lensing signal by unlensed cluster members; if not thoroughly excluded, this contamination will reduce the lensing signal preferentially towards the cluster center, resulting in a flatter mass profile, as pointed out by Broadhurst et al. (2005b).

Another well studied cluster that we use here is Cl0024-17 ($z = 0.395$), with an effective Einstein radius of $31''$ at $z = 1.7$ defined by several sets of multiple images identified in the ACS/GTO images. This agrees in particular with the mean radius of the famous 5-image system of “ θ ” arcs at a spectroscopically measured redshift of $z = 1.685$ (Broadhurst et al. 2000). This set of multiple images and the distortion measurements of background galaxies with photometric redshifts has been used by Jee et al. (2007) to constrain the inner mass profile. Their result is in general consistent in form with the earlier analysis of the inner profile by Broadhurst et al. (2000), but with the addition of a narrow low-contrast ring that, it is claimed, can be reproduced in simulations where merging of two massive clusters occurs along the line of sight. A line-of-sight merger is also blamed for the relatively small central velocity dispersion (Czoske et al. 2002). However, in the extensive weak lensing analysis of Kneib et al. (2003) only one small subgroup is

visible, offset by $3'$ in projection from the center of mass and accounting for only $\sim 15\%$ of the total mass of the cluster. Kneib et al. (2003) find that the main cluster is well fitted by an NFW profile with a virial mass of $\sim 6 \times 10^{14} M_\odot/h$ and with a high concentration, $c_{\text{vir}} \sim 20$. In a more recent analysis of deep multicolour B,R,Z Subaru images, Medezinski et al. (2007, in preparation) find good agreement with Kneib et al. (2003) (Table 1).

In addition, we use the very deep ACS/GTO images of the massive cluster A1703 for which many sets of multiple images are visible, so that the tangential critical line is easily identified with a mean Einstein radius of $32''$ at $z = 2.8$, in good agreement with the radius of the main giant arc at a similar redshift (Table 1). In the weak lensing analysis of Medezinski et al. (2007, in preparation) a very good fit to an NFW profile is found with a virial mass $M_{\text{vir}} = 7 \times 10^{14} M_\odot/h$. This cluster appears relaxed and centrally concentrated, with little obvious substructure. To date, deep X-ray imaging is unfortunately missing.

Finally, a weak lensing analysis of RXJ1347 (Medezinski et al. 2007, in preparation) shows this cluster to have a very circular shear pattern, with an estimated virial mass $M_{\text{vir}} = 9 \times 10^{14} M_\odot/h$ based on an NFW fit to the radial distortion profile. This cluster has the highest observed X-ray temperature of 13 keV and a symmetric X-ray emission map that indicates that it is relaxed (Vikhlinin et al. 2002). A very symmetric distribution of arcs is visible around the cluster center, implying a well-determined Einstein radius at $z = 1.8$ of $35''$ from the full model, a value which is also in agreement with a system of 5 multiply-lensed images at this redshift (Halkola et al. 2008).

These four clusters are particularly useful for our purpose, by virtue of their well-defined Einstein radii and precise measurements of the virial masses, which allows a comparison with the theoretical predictions as a function of halo mass. We convert M_{vir} to M_{200} for each cluster using the measured value of c_{vir} , and adopt error bars of $\pm 15\%$ on M_{200} and $\pm 10\%$ on θ_E for all four clusters (but see the next subsection for an alternative measurement of the virial mass of A1689). It is also interesting to note the many examples of strong lensing by other galaxy clusters for which the total mass is not so well constrained. Samples of clusters defined by some reasonable criteria (Smith et al. 2005; Sand et al. 2005; Comerford et al. 2006) show that invariably the observed Einstein radius (when detected) for intermediate redshift clusters does not fall short of $10''$, with a mean of $\sim 15''$. This may be compared with the predicted typical Einstein radius of only $\sim 5''$ from the simulations of Neto et al. (2007) and Hennawi et al. (2007) for a cluster of $M_{200} = \text{several} \times 10^{14} M_\odot$ (Figure 2).

2.3 Model-Independent Mass

Of the two observational quantities we use to characterize each cluster, θ_E is more directly estimated, from the positions of multiple images. The mass M_{200} requires a measured mass profile out to large angles, which can be used to estimate the angular position corresponding to r_{200} , i.e., to an enclosed relative density of 200 times the critical density. Deep images provide a large density of weakly-lensed background sources, but weak lensing distortions measure only the reduced shear and suffer from the well-known mass-

sheet degeneracy. This means that the mass profile can be measured without degeneracies only by fitting a particular parametrized density profile model to the data. However, combining lensing distortions with observations of the variation in the number density of background sources due to weak magnification breaks the degeneracy and yields a direct measurement of the projected surface density in each radial bin (Broadhurst et al. 2005b). Given such independent measurements out to large radius, we can derive the corresponding value of M_{200} directly from the data, without the intermediary of an assumed model profile, the use of which inevitably introduces a non-trivial systematic error. Such accurate measurements are available for A1689, which we use to illustrate the method, and such data should be obtainable for other clusters as well. We note that this effective virial mass is defined from deprojecting the projected mass assuming spherical symmetry, which is the closest lensing observations can come to the standard theoretical definition of the virial mass based on a 3-D spherical average.

Lensing by a halo can be analyzed by calculating $\kappa = \Sigma/\Sigma_{\text{cr}}$. The projected surface density is related to the three-dimensional density ρ by an Abel integral transform. This implies a relation between the integrated three-dimensional mass $M(r)$ out to radius r and $\kappa(R)$ as a function of the projected radius R :

$$M(r) = \Sigma_{\text{cr}} \left[2\pi \int_0^r R \kappa(R) dR - 4 \int_r^\infty R \kappa(R) f\left(\frac{R}{r}\right) dR \right], \quad (8)$$

where

$$f(x) = \frac{1}{\sqrt{x^2 - 1}} - \tan^{-1} \frac{1}{\sqrt{x^2 - 1}}. \quad (9)$$

The first term in equation (8) is the total projected mass within a ring of projected radius r , and the second term removes the contribution from mass elements lying at a 3-D radius greater than r .

To obtain the 3-D mass profile $M(r)$, we apply equation (8) to the 26 values of $\kappa(R)$ measured by Broadhurst et al. (2005b) over the range $R = 0.015 - 2.3$ Mpc in A1689. Specifically, we linearly interpolate $\kappa(R)$ between each pair of measured points, and extrapolate outside the range. We extrapolate inward assuming $\kappa(R) = \text{const}$ from the innermost point and outward assuming $\kappa(R) \propto R^{-2}$ from the outermost point, where these power laws are motivated by the NFW profile. However, even varying these powers by ± 1 would change the virial mass by only 1%, which is negligible compared with the effect of the measurement errors. Once we have obtained $M(r)$ at all r , we interpolate to find the appropriate r that yields a desired mean enclosed density, and thus determine the virial radius and mass. The error analysis is complicated by the fact that the virial radius is not fixed but rather is itself determined by the data. Thus, to ensure self-consistent errors we use a Monte Carlo approach, generating 1000 random profiles of $\kappa(R)$ according to the measurement errors (assumed to be Gaussian distributed except that κ is constrained to be non-negative). For each $\kappa(R)$ profile we find the resulting virial quantities, and then find the 16%, 50% (median), and 84% percentiles. The result of this direct, model-independent analysis of A1689 is:

$$r_{\text{vir}} = 2.76 \pm 0.2 \text{ Mpc}, \quad M_{\text{vir}} = (1.6 \pm 0.4) \times 10^{15} M_\odot,$$

$$r_{200} = 2.25 \pm 0.2 \text{ Mpc}, \quad M_{200} = (1.5 \pm 0.4) \times 10^{15} M_\odot.$$

The median value obtained for M_{200} is lower by $\sim 15\%$ than the best-fit value from the NFW profile. This is consistent with our model-independent analysis of A1689 in Lemze et al. (2007), where we found that the NFW fit clearly overshoots the observed density profile at large radii. Also, the model-independent error of $\sim 25\%$ is larger since assuming an NFW profile puts a constraint on the density fluctuations and yields a reduced error. The 25% error results from allowing completely independent variations in the κ measurements at different radii, so the error would be reduced with even a weak assumption of smoothness in the density profile. Here we adopt the model-independent mass along with its conservatively large 25% error (Table 1). The model-independent mass is the most reliable observationally-determined mass and is more consistent with a comparison to numerical simulations, where the real virial masses are known without the need to resort to profile fitting.

The most important assumption in our analysis is spherical symmetry. Since the measured κ profile goes out to $\sim r_{200}$, what we directly measure includes the full contribution of M_{200} plus additional projected mass coming from larger radii. If the halo has non-spherical structure such as triaxiality, then lensing bias means that the contribution of mass elements outside the virial radius to the projected mass will tend to be unusually high in our direction. However, since we get that contribution by extrapolating from the measured κ points (which are also enhanced by lensing bias), the error in our spherical assumption may be small. The real conclusion is that since the 3-D virial mass is not directly observable, lensing analyses of halos in numerical simulations should measure the effective, projected ‘virial’ mass defined by applying equation (8) to the projected profile. This would allow a truly direct comparison with the observations.

3 CONFRONTING Λ CDM WITH OBSERVATIONS

For each cluster with known redshifts z_L and z_S and a reliably measured value of M_{200} , we can use the results of section 2.1 to calculate the predicted value of θ_E in the Λ CDM model. Figure 3 compares the median expected value with the observed value for each cluster, showing that in each case the theoretical expectation falls short of the observed value by about a factor of two. Specifically, the predicted Einstein radii are $24''$, $15''$, $16''$, and $23''$, for A1689, Cl0024, A1703, and RXJ1347, respectively. In this Figure we also separately illustrate the dependence of the predicted θ_E on the source and lens redshifts. In general, the predicted θ_E increases with z_S , with the dependence weakening as z_S moves further away from z_L . For a fixed z_S , θ_E is maximized at a particular value of z_L , which for the z_S values of our three clusters falls at z_L between 0.4 and 0.6. The overall dependence of θ_E is weak, illustrating that the discrepancy between the theory and the observations would not be significantly affected by small changes in the redshifts.

The results of section 2.1 allow us to make a much more detailed study of the large Einstein radius problem. We show in Figure 4 the full predicted probability distribution of θ_E for each cluster. The main predictions (solid

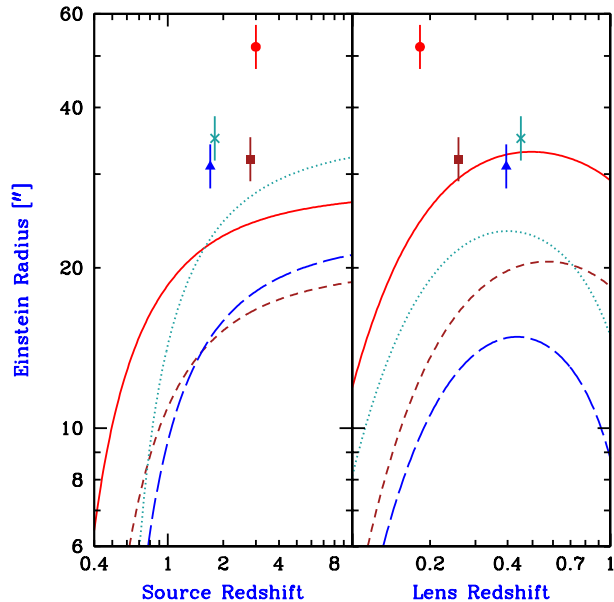


Figure 3. Dependence of the Einstein radius θ_E on the redshifts z_S (left panel) and z_L (right panel). We consider A1689 (solid curves, circles), A1703 (short-dashed curves, squares), Cl0024 (long-dashed curves, triangles), and RXJ1347 (dotted curves, \times 's). In each case, the points correspond to the observed cluster (with a vertical bar indicating the measurement error), while the curves show the predicted θ_E based on the median c_{200} of relaxed simulated halos as measured by Neto et al. (2007) in the nearest mass bin, after correction for lensing and projection bias based on Figure 1.

curves) yield probabilities of 1.5%, 0.56%, 5.0%, and 3.7% for finding a cluster with as large a value of θ_E (given the redshifts) as observed for A1689, Cl0024, A1703, and RXJ1347, respectively. In this Figure and the previous one, we have used the relaxed halo population from Neto et al. (2007). As the Figure shows, including the unrelaxed halos would only strengthen the inconsistency with the observations. The results from Neto et al. (2007) are uncertain due to the relatively small halo samples used. Specifically, since $\log_{10} c_{200}$ is Gaussian distributed, the fractional sampling error with $N \gg 1$ halos is $1/\sqrt{N}$ in the measurement of the mean of the distribution and $1/\sqrt{2N}$ in the standard deviation. Figure 4 shows the result of increasing the standard deviation by its $1-\sigma$ sampling error; increasing the mean by its $1-\sigma$ error would have a smaller effect. While larger simulations will reduce the sampling noise, the Figure shows that this uncertainty is already smaller than the effect of the measurement errors in the cluster masses.

Including the rather conservative observational uncertainties that we have assumed in M_{200} and θ_E , and averaging over Gaussian error distributions in these two observables, we obtain probabilities of 8.5%, 3.9%, 7.9%, and 13%, for agreement between the Λ CDM simulations and A1689, Cl0024, A1703, and RXJ1347, respectively. If we considered just one of the clusters, the large Einstein radius problem would only constitute around a $2-\sigma$ discrepancy. However, we have four independent objects selected from the population of cluster lenses, and all four are discrepant (in the same direction). The total probability of the theoretical pre-

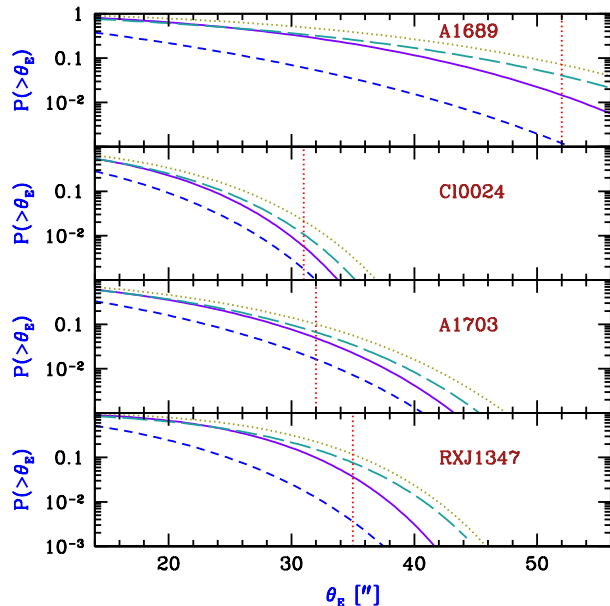


Figure 4. Cumulative probability distribution $P(> \theta_E)$, assuming the lognormal c_{200} distribution measured by Neto et al. (2007) for halos from a numerical simulation. We consider A1689, C10024, A1703, and RXJ1347 as indicated, assuming in each case the best-fit mass from observations, and the c_{200} distribution as measured from the simulation for the nearest mass bin of relaxed halos (solid curves). We also consider several possible sources of statistical or systematic error, and we illustrate the result of assuming a cluster mass higher by the $1\text{-}\sigma$ measurement error (dotted curves), or a scatter $\sigma_{\log_{10} c_{200}}$ higher by the $1\text{-}\sigma$ sampling noise (see text; long-dashed curves). In all cases shown, $P(> \theta_E)$ for unrelaxed halos would lie below the corresponding curve for relaxed halos, throughout the plotted region. Thus, we only illustrate the main case with the c_{200} distribution as measured for unrelaxed halos (short-dashed curves). Also shown for comparison for each cluster (dotted vertical line) is the observed θ_E .

diction yielding four clusters with such large values of θ_E is 3×10^{-5} , which corresponds to a $4\text{-}\sigma$ discrepancy. We emphasize that we have included in this calculation the lensing and projection biases, as well as the measurement errors in the cluster masses and Einstein radii.

4 DISCUSSION

We have presented perhaps the clearest, most robust current conflict between observations and the standard Λ CDM model. This model is highly successful in fitting large scale structure measurements, which in turn strongly constrain the free parameters of the model and thus produce precise predictions for comparison with data on smaller scales. Structure on these scales is non-linear and potentially affected by gas physics, but clusters provide perhaps the best opportunity for a robust comparison between the models and the theory. Clusters are so large and massive that their evolution is dominated by gravity, especially since their high virial temperature prevents most of the intracluster gas from cooling. The evolution of clusters including gravitational collapse and virialization can now be accurately numeri-

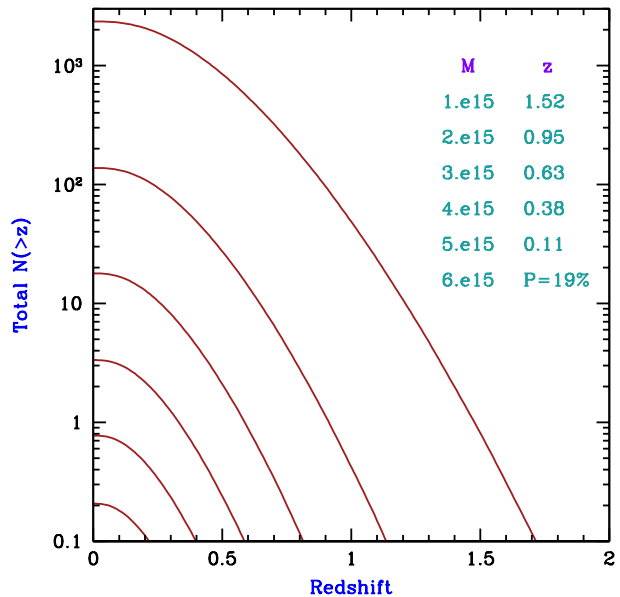


Figure 5. Total number of observable clusters in the universe above redshift z , obtained by integrating the halo mass function of Sheth, Mo, & Tormen (2001) over our past light cone. We consider all cluster halos above virial mass $M = 1, 2, 3, 4, 5$, or $6 \times 10^{15} M_\odot$ (top to bottom). Also listed for each M (top-right corner) is the redshift above which there is a 50% chance of observing at least one halo of mass greater than M . For $M = 6 \times 10^{15} M_\odot$ we instead list the probability of observing at least one halo at any $z > 0$.

cally simulated, with sufficient resolution for studying cluster structure and for simulating lensing in projection, and in sufficient volumes to produce large samples in a cosmological context. At the same time, observations of clusters combining weak and strong lensing now produce accurate virial mass determinations. Given the virial mass, the cleanest measure of the halo structure is the effective Einstein radius, which is easily obtained observationally from a model constrained by large numbers of arcs and directly measures the central mass density.

We derived the theoretical predictions for cluster lensing in Λ CDM using the distribution of 3-D halo profiles measured by Neto et al. (2007) in the Millennium simulation, after correcting it for lensing and projection biases based on Hennawi et al. (2007). These analyses of numerical samples expressed halo structure in terms of the NFW concentration parameter. We found two key results (Figure 1) based on the halo analysis by Hennawi et al. (2007): first, that the distribution of 3-D concentrations of the lens population is the same as that of the general halo population except for a shift upwards by a factor of 1.17; and second, that the concentrations measured in projection are related to the 3-D concentrations, such that the ratio follows a lognormal distribution which corresponds to a factor of 1.14 shift plus a factor of 1.33 spread. The concentration parameter is higher for relaxed halos than for unrelaxed, and it declines slowly with halo mass, resulting in a predicted Einstein radius that increases roughly linearly with mass for relaxed halos (Figure 2).

We compared the theoretical predictions with the ob-

served θ_E for four clusters, A1689, Cl0024, A1703, and RXJ1347. For the latter three we used the virial mass as given by NFW fits to the lensing observations, but for A1689 we obtained a model-independent mass directly from the lensing data, only assuming spherical symmetry (section 2.3). For each object, the predicted θ_E values came up short by a factor of two compared with the observations (Figure 3). After including the measurement errors, the full probability distribution functions of the predicted Einstein radii excluded the theoretical model at $2\text{-}\sigma$ for each object. The total probability of the standard Λ CDM model yielding four clusters with such large θ_E is 3×10^{-5} , a $4\text{-}\sigma$ discrepancy.

Lensing work is now being extended to larger samples of clusters, so that in the near future we may examine more fully the relation between the Einstein radius and virial mass and its scatter, over a wider range of cluster masses. The theoretically predicted triaxiality of CDM halos implies a particular scatter in the projected concentration parameter (and thus in the Einstein radius) for a given halo mass. This scatter, which we included in our calculations, is apparently insufficient to explain the observations. If the scatter is observationally determined to be relatively small, then this would further highlight the problem we have discussed and leave the high concentrations unexplained. Determining the scatter observationally will also statistically probe the degree of triaxiality of CDM halos. To ensure the most direct, unbiased comparison, the simulated distributions should be calculated not at a fixed 3-D virial mass, but at a fixed projected, effective virial mass, defined as in section 2.3.

Numerical simulations show a clear correlation between the concentration of a halo and its formation time, i.e., the time at which a significant portion of the halo mass first assembled (e.g., Neto et al. 2007). This agrees with the intuitive notion that a dense halo core must have assembled at high redshift, when the cosmic density was high. Thus, the fact that observed cluster halos are apparently more centrally concentrated than is predicted in Λ CDM suggests an additional mechanism that promotes the collapse of cluster cores at an earlier time than expected. Baryons are unlikely to help. Central cD galaxies contribute only a small fraction of the mass within the Einstein radius, which for our three clusters is ~ 150 kpc enclosing a projected mass of $\sim 2 \times 10^{14} M_\odot$, or a 3-D mass of $\sim 1 \times 10^{14} M_\odot$. We can estimate the effect of baryons on the total mass profile using the simple model of adiabatic compression (Blumenthal et al. 1986). Within this model, conservation of angular momentum implies that the quantity $rM(r)$ (assuming spherical symmetry) is fixed. Assuming that we start out with a halo with the mean expected theoretical concentration (Figure 2), the observed 3-D mass within the Einstein radius can be obtained through adiabatic compression if the enclosed baryonic mass within this radius is $\sim 3 \times 10^{13} M_\odot$ in the three clusters we considered. Thus, explaining the discrepancy through adiabatic compression requires the baryonic fraction within the Einstein radius to be $\sim 1/3$, twice the cosmic baryon fraction. This seems highly unlikely, as the observed X-ray emission yields at these radii gas fractions well below the cosmic value (e.g., see Figure 12 of Lemze et al. (2007) for A1689), and a cD galaxy contains only $\sim 1 \times 10^{12} M_\odot$ in baryons (e.g., see Matsushita et al. (2002) for M87).

Modifications in the properties of dark matter or the slope of the primordial power spectrum are generally expected to have a smaller effect on clusters than on smaller-scale objects which are predicted in Λ CDM to have earlier formation times and higher concentrations. On the other hand, since clusters are rare objects in the standard model, primordial non-Gaussianity would significantly affect them and allow clusters to form earlier, which may also help explain other observations (Mathis et al. 2004; Sadeh et al. 2007). Regardless of the mechanism, early collapse of cluster cores may have observable consequences if it is accompanied by star formation.

Finally, we note that the fact that clusters are now being detected with masses $\sim 10^{15} M_\odot$ is completely consistent with the Λ CDM model. Indeed, Figure 5 shows that large numbers of clusters are expected out to significant redshifts, including $M = 2 \times 10^{15} M_\odot$ halos out to $z \sim 1$, as well as more massive halos up to $\sim 5 \times 10^{15} M_\odot$ at lower redshift. Clearly, while large samples of halos with precise, profile-independent lensing determinations of both θ_E and M_{vir} will make our results completely conclusive, the highly-significant discrepancy we have identified already represents a substantial challenge for Λ CDM.

ACKNOWLEDGMENTS

We thank Masataka Fukugita and Masahiro Takada for useful discussions. RB is grateful for support from the ICRR in Tokyo, Japan and from the John Simon Guggenheim Memorial Foundation. We acknowledge Israel Science Foundation grants 629/05 (RB) and 1218/06 (TJB).

REFERENCES

- Astier, P., et al. 2006, *A&A*, 447, 31
- Bartelmann, M. 1996, *A&A*, 313, 697
- Blumenthal, G. R., Faber, S. M., Flores, R., & Primack, J. R. 1986, *ApJ*, 301, 27
- Bradač, M., et al. 2007, *ArXiv e-prints*, 711, arXiv:0711.4850
- Broadhurst, T., Huang, X., Frye, B., & Ellis, R. 2000, *ApJ*, 534, L15
- Broadhurst, T., et al. 2005a, *ApJ*, 621, 53
- Broadhurst, T., Takada, M., Umetsu, K., Kong, X., Arimoto, N., Chiba, M., & Futamase, T. 2005b, *ApJ*, 619, L143
- Bryan G. L., & Norman M., 1998, *ApJ*, 495, 80
- Bullock J. S., Kolatt T. S., Sigad Y., Somerville R. S., Kravtsov A. V., Klypin A. A., Primack J. R., & Dekel A., 2000, *MNRAS*, 321, 559
- Comerford, J. M., Meneghetti, M., Bartelmann, M., & Schirmer, M. 2006, *ApJ*, 642, 39
- Czoske, O., Moore, B., Kneib, J.-P., & Soucail, G. 2002, *A&A*, 386, 31
- Diego J. M., Sandvik H. B., Protopapas P., Tegmark M., Benítez N., & Broadhurst T. 2005, *MNRAS*, 362, 1247
- Ford, H. C., et al. 1998, *procSPIE*, 3356, 234
- Gao, L., et al. 2007, *MNRAS*, submitted (arXiv:0711.0746)
- Gavazzi, R., Fort, B., Mellier, Y., Pelló, R., & Dantel-Fort, M. 2003, *A&A*, 403, 11

- Gioia, I. M., Maccacaro, T., Schild, R. E., Wolter, A., Stocke, J. T., Morris, S. L., & Henry, J. P. 1990, *ApJS*, 72, 567
- Halkola A., Hildebrandt H., Schrabback T., Lombardi M., Bradac M., Erben T., Schneider P., Wuttke D., 2008, *A&A*, in press
- Halkola, A., Seitz, S., & Pannella, M. 2006, *MNRAS*, 372, 1425
- Hennawi J. F., Dalal N., Bode P., & Ostriker J. P., 2007, *ApJ*, 654, 714
- Jee, M. J., et al. 2007, *ApJ*, 661, 728
- Kaiser, N., Squires, G., & Broadhurst, T. 1995, *ApJ*, 449, 460
- Kling, T. P., Dell’Antonio, I., Wittman, D., & Tyson, J. A. 2005, *ApJ*, 625, 643
- Kneib, J.-P., et al. 2003, *ApJ*, 598, 804
- Lemze D., Barkana R., Broadhurst T. J., & Rephaeli Y. 2007, *MNRAS*, accepted
- Limousin, M., et al. 2007, *ApJ*, 668, 643
- Mathis H., Diego J. M., & Silk J. 2004, *MNRAS*, 353, 681
- Matsushita, K., Belsole, E., Finoguenov, A., Böhringer, H. 2002, *A&A*, 386, 77
- Medezinski, E., et al. 2007, *ApJ*, 663, 717
- Navarro J. F., Frenk C. S., & White S. D. M. 1997, *ApJ*, 490, 493 (NFW)
- Neto, A. F., et al. 2007, *MNRAS*, 381, 1450
- Oguri M., Takada M., Umetsu K., & Broadhurst T. 2005, *ApJ*, 632, 841
- Percival, W. J., Cole, S., Eisenstein, D. J., Nichol, R. C., Peacock, J. A., Pope, A. C., & Szalay, A. S. 2007, *MNRAS*, 381, 1053
- Sadeh S., Rephaeli Y., & Silk J. 2007, *MNRAS*, 380, 637
- Sand D. J., Treu T., Ellis R. S., & Smith G. P. 2005, *ApJ*, 627, 32
- Sheth R. K., Mo H. J., & Tormen G. 2001, *MNRAS*, 323, 1
- Smith, G. P., Kneib, J.-P., Smail, I., Mazzotta, P., Ebeling, H., & Czoske, O. 2005, *MNRAS*, 359, 417
- Spergel D. N. et al. 2007, *ApJS*, 170, 377
- Umetsu, K., & Broadhurst, T. 2008, submitted (arXiv:0712.3441)
- Vikhlinin, A., VanSpeybroeck, L., Markevitch, M., Forman, W. R., & Grego, L. 2002, *ApJ*, 578, L107
- Williams, L. L. R., Navarro, J. F., & Bartelmann, M. 1999, *ApJ*, 527, 535
- Zekser K. C. et al. 2006, *Apj*, 640, 639